Optical Materials: X 24 (2024) 100368

Contents lists available at ScienceDirect

Optical Materials: X

journal homepage: www.journals.elsevier.com/optical-materials-x

Low temperature recombination luminescence of $Mg_3Y_2Ge_3O_{12}:Tb^{3+}$

U. Rogulis *, A. Fedotovs, Dz Berzins, G. Krieke, L. Skuja, A. Antuzevics

Institute of Solid State Physics, University of Latvia, 8 Kengaraga str., LV-1063, Riga, Latvia

A R T I C L E I N F O

Keywords:
$Mg_3Y_2Ge_3O_{12}:Tb^{3+}$
Photoluminescence
Afterglow
Electron paramagnetic resonance
Paramagnetic centres
Recombination mechanism

A B S T R A C T

A study was conducted to examine the recombination processes in persistent phosphor $Mg_3Y_2Ge_3O_{12}:Tb^{3+}$ garnet at low temperatures. Photoluminescence (PL), recombination luminescence (RL), electron paramagnetic resonance (EPR), and EPR detected by PL or RL were measured.

In samples with low Tb^{3+} concentration, a broad PL and RL band around 400–450 nm and characteristic Tb^{3+} lines were observed. However, in samples with high Tb^{3+} concentration, only Tb^{3+} lines were present. Both the broad-band and the line components exhibit long-lasting tunneling luminescence with hyperbolic decay. After 263 nm UV irradiation signals of intrinsic electron (F-type) and hole (V-type) trapping centres were observed in the EPR spectra. Such signals were also observed in RL-detected EPR spectra, indicating that the broad RL band at low Tb^{3+} concentrations originates from tunneling recombination between these intrinsic traps. At high Tb^{3+} concentrations, the RL-EPR spectrum was not observed, suggesting that intrinsic electron and Tb-related hole trapping centres probably participate in the tunneling recombination.

1. Introduction

Persistent phosphors have a wide range applications in various fields such as security signs, luminous paints and displays [1–3], luminescence imaging of biological systems [4,5], photodynamic therapy [6,7] and others. Complex oxide garnets is a wide material class for persistent luminescence and other optical applications, in which defects, intrinsic and extrinsic luminescence [8–12] and recombination processes [13,14] have been investigated.

Tb^{3+} ion-activated $Mg_3Y_2Ge_3O_{12}$ (in the following text - MYG) garnet is a promising new blue to green tuneable persistent phosphor at room temperature [15]. MYG has a well-elucidated structure of inverse garnet [16], with band gap E_g in the range of 5.52–5.54 eV determined with the diffuse reflectance method at room temperature [17,18]. Doping MYG with Sm^{3+} [17], Bi^{3+} and Eu^{3+} [18] has prospective applications as red-emitting phosphors for white LEDs. Bi-doped MYG as a UV phosphor may act as a “sensitizer” in the process of reducing the viscosity of heavy oil [19]. MYG doped with Ce^{3+} yields a yellow phosphor [20] and has been proposed as a persistent luminescence anti-flicker material for alternating current light emitting diodes [21].

In previous research, formation of several hole-type charge traps have been detected in MYG:Tb, but the mechanism of this tuneable persistent phosphor has not been fully explained [15]. There are no studies at low temperatures that could provide a more comprehensive understanding of the optical processes involved in MYG:Tb.

Low temperatures have often proven to be highly beneficial in the study of recombination mechanisms. The possibility of using the recombination luminescence detected EPR (RL-EPR) method appears at lower temperatures, which allows direct identification of the EPR-active centres participating in the recombination process [22–24]. Additionally, RL-EPR is usually performed at higher microwave frequencies (up to 60–95 GHz) and correspondingly higher magnetic fields, which increases the resolution compared to EPR’s most common microwave frequency range of 9 GHz [23,24]. To our knowledge, no RL-EPR techniques have been applied to complex oxide compounds similar to MYG: Tb. We recently applied the RL-EPR to investigate the low-temperature recombination luminescence in La-doped Ca_2SnO_4 which allowed to get inside to recombination processes of this material [25].

This work reports recombination luminescence (RL) studies at low temperatures, involving also the RL-EPR method in the long-lasting afterglow of MYG:Tb, performed with an aim of elucidating the nature of paramagnetic centres participating in recombination processes at low and high Tb concentrations.

2. Materials and methods

MYG samples with a general formula of $Mg_3Y_{2-x}Ge_3O_{12}$: xTb^{3+} (x = 0.0002; 0.2 corresponding to MYG:0.01 % and MYG:10 % (mol%)) were

* Corresponding author.
E-mail address: uldis.rogulis@cfi.lu.lv (U. Rogulis).

https://doi.org/10.1016/j.omx.2024.100368
Received 8 July 2024; Received in revised form 17 September 2024; Accepted 25 September 2024
Available online 26 September 2024

prepared using high-temperature solid-state synthesis. Detailed synthesis parameters have been described previously [15].

The powder particle sizes determined by the SEM method were approximately 1–4 µm. The phase composition of the prepared samples was analysed by X-ray diffraction (XRD) using Rigaku MiniFlex 600. Cu K-α radiation from X-ray lamp operated at 40 kV and 15 mA was used.

For photoluminescence (PL) and RL measurements, wavelength-tuneable pulsed solid-state laser Ekspla NT342/3UV was used as an excitation source. The signal was detected using Andor Shamrock B-303i spectrometer coupled with Andor iSTAR DH734 CCD camera. Optical measurements were carried out at 10–300 K using Advanced Research Systems DE202 N cold finger-type helium cryostat. The thermo-stimulated luminescence (TSL) heating rate was 10 K/min.

PL- and RL-excitation measurements in the spectral range 200–375 nm were carried out at 10 K using Edinburg Instruments FLS1000spectrometer equipped with Janis Research SHI-950-5 optical closed cycle refrigerator with sample in an exchange gas. The intensity measurements were corrected for the spectral response of the spectrometer. The efficiency of RL excitation was evaluated by measuring the difference in the afterglow amplitude between 30 and 60 s after 30 s UV excitation in order to eliminate possible small background from the previous measurement point.

The Bruker ELEXSYS-II E500 CW-EPR spectrometer was used for electron paramagnetic resonance (EPR) investigations of the samples. The spectra acquisition settings were as follows: 40 K, 9.357 GHz microwave frequency, 0.1 mT magnetic field modulation amplitude with 100 kHz modulation frequency, and 0.1 mW microwave power unless specified otherwise. EPR spectra were obtained after exposing the sample to two different ultraviolet (UV) irradiation settings: (1) 230 nm excitation at room temperature outside the EPR resonator; (2) 263 nm excitation maintaining the sample at 40 K within the EPR resonator. EPR spectra were analysed using the Easyspin software toolbox for Matlab [26] employing the following spin-Hamiltonian (SH):

$$H = g\mu_B BS \quad (1)$$

where g is the g-factor; μ_B – the Bohr magneton; B – external magnetic field; S – electronic spin operator [27]. During the simulation process, the g-factor components were changed to achieve the best fit to experimental spectra.

Photoluminescence detected EPR (PL-EPR) and RL-EPR were measured using a custom-built spectrometer with an Oxford Instruments liquid helium cryostat at microwave frequencies of 62.0 GHz (V-band) and 97.9 GHz (W-band) at a temperature of 1.5 K.

PL and RL were excited using a xenon lamp with a 250 nm UV bandpass filter with 40 nm bandwidth and detected with a Hamamatsu photomultiplier tube in the spectral range from 200 to 900 nm.

RL-EPR was detected in the integral afterglow luminescence after UV irradiation for approximately 5 min at T = 1.5 K. The magnetic field-dependent background was subtracted.

PL-EPR was measured via a 310–780 nm bandpass filter using microwave modulation and a lock-in amplifier operating at 1 Hz frequency.

3. Results and discussion

3.1. X-ray diffraction

The phase composition of the MYG:Tb samples was analysed using X-ray diffraction analysis. The XRD pattern matches with the standard diffraction lines of MYG garnet (PDF 01-089-6603); no additional peaks were noticed (see Fig. 1), indicating that the samples contain single-phase garnet-type MYG and the Tb^{3+} is incorporated in the crystalline lattice. The results are consistent with our previous work, which demonstrated unlimited solubility of Tb^{3+} in the MYG lattice [15].

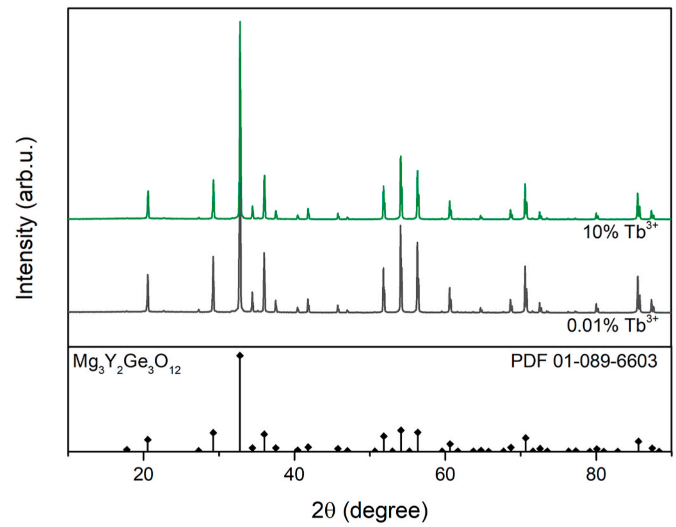

Fig. 1. XRD patterns of the MYG garnet samples doped with 0.01 and 10 mol % Tb^{3+}.

3.2. Luminescence

Low-temperature photoluminescence spectra of the MYG:Tb garnet samples were measured for two Tb^{3+} concentrations – 0.01 % and 10 % Tb^{3+}.

In the 0.01 % Tb^{3+} concentration sample, a broad PL band with a maximum at about 380 nm is observed using 210 nm excitation (Fig. 2a, dotted curve). At the excitation at 250 nm, the broad band maximum is shifted to about 450 nm and multiple narrow luminescence bands in the 360–700 nm range associated with $^5D_3 \rightarrow {}^7F_J$ and $^5D_4 \rightarrow {}^7F_J$ transitions of Tb^{3+} could be detected (Fig. 2a, solid curve). It should be noted that this broad emission band is also present in undoped samples. The broad band PL excitation (PLE) spectra have a maximum at about 207 nm (Fig. 2a, dashed curve). No significant deviations were detected in PLE spectra of this band when measured at different spectral positions. The intensity of the broad PL band is the highest at low temperatures and decreases upon increasing temperature (Fig. 2b). The origin of broad emission band is discussed further in this work.

After switching off the excitation source, a long-lasting RL was observed for the 0.01 % Tb^{3+} doped MYG sample (Fig. 3). After the 210 nm excitation (dotted curve), a broad RL band with a maximum at about 425 nm was observed with overlapping Tb^{3+} lines. At the excitation at 250 nm (solid curve), the broad band maximum is located at about 450 nm with about the same Tb^{3+} line intensities. The broad-band RL excitation (RLE) efficiency after 30 s excitation and measured intensity difference between 30 and 60 s is shown in Fig. 3 as well (dashed curve). Both the broad-band PL and RL in MYG could be excited by approaching and exceeding the band-gap value of 5.53 eV (225 nm - at room temperature, at low temperatures it should be at somewhat shorter wavelengths). This indicates that electrons and holes created by band-band transition bind/recharge to electron-hole centres, which then gives broad-band PL/RL.

For the high Tb concentration of 10 %, both the PL and RL spectra show several sharp and narrow emission bands located at 490 nm, 543 nm, 583 nm, 625 nm and 667 nm lines which correspond to $^5D_4 \rightarrow {}^7F_6$, $^5D_4 \rightarrow {}^7F_5$, $^5D_4 \rightarrow {}^7F_4$, $^5D_4 \rightarrow {}^7F_3$, $^5D_4 \rightarrow {}^7F_2, {}^7F_1$ transitions of Tb^{3+} respectively (Fig. 4, if normalized, all shapes practically coincide). No evidence of the broad PL or RL band has been observed. Two broad excitation peaks were observed in the PLE spectra while monitoring the 544 nm emission, with maxima at 280 nm and 317 nm. The strongest excitation peak, centred at 272 nm, is attributed to 4f-5d transitions of Tb^{3+}, consistent with previous findings in similar materials [28–30]. The 317 nm peak has been previously reported in $Mg_3Y_2Ge_3O_{12}$ and is thought to

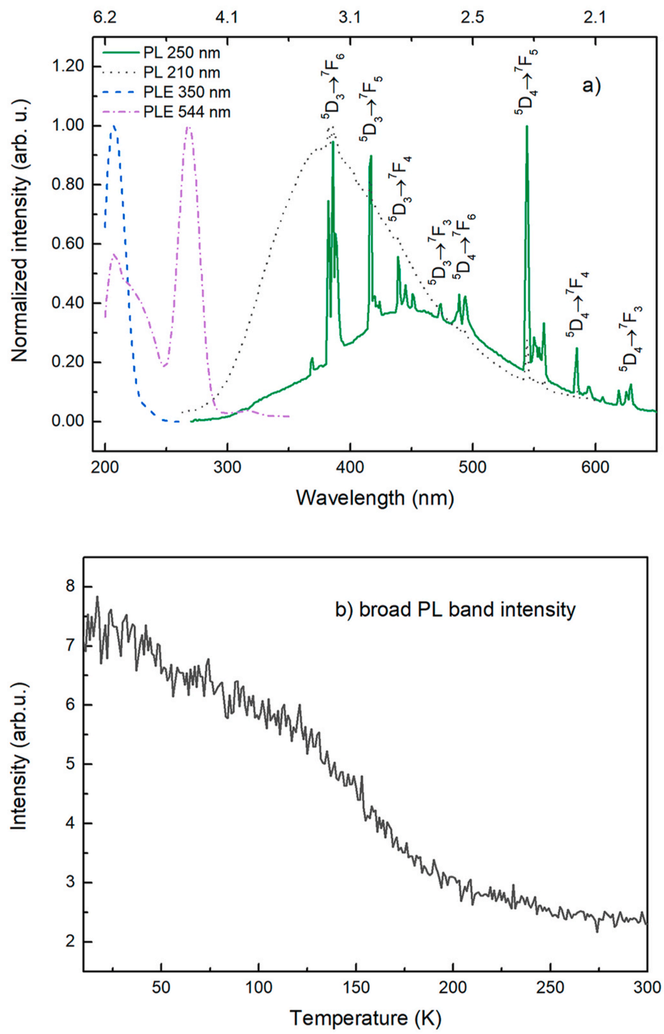

Fig. 2. PL characteristics of the MYG garnet doped with 0.01 % Tb^{3+}: a) excited at 210 nm (dotted curve), 250 nm (solid curve), excitation spectra for emission at 350 nm (dashed curve) and 544 nm (dashed-dotted curve) at temperature 10 K and b) temperature dependence of the broad PL band.

be either due to f-d transitions of Tb^{3+} in a distorted environment or associated with point defects [15]. Similarly as for the low Tb concentration sample, RL could be excited by photons with energies close to the value of MYG band gap. For the 10 % Tb sample, the RL in lower extent could be excited going through the 4f→5d excitation band of the Tb^{3+}.

Integral RL decay kinetics of MYG:Tb are shown in Fig. 5 for low (0.01 %) and high (10 %) Tb^{3+} concentrations. Long-lasting hyperbolic decay, which is linear in double-logarithmic coordinates, has been observed for both Tb^{3+} concentrations. Hyperbolic decay is characteristic for tunneling recombination between spatially distributed electron and hole trap centre pairs [31,32]. The starting points of the kinetics could be lower than the straight line due to the relatively long excitation time.

After the UV excitation at T = 10 K, both low- (0.01 % Tb, Fig. 6a) and high-doped (10 % Tb, Fig. 6b) MYG samples exhibit a low-temperature TSL peaks with the maximum at about 65 K.

TSL for the 0.01 % doped sample is shown to start at about 25 K, which, in addition to the hyperbolic decay kinetics mentioned earlier, indicates that RL occurs as the tunneling recombination. For the 10 % Tb sample, TSL starts at about 20 K and hyperbolic decay kinetics behaviour indicate the tunneling recombination process in the RL as well. Moreover, for RL at both low and high Tb concentrations, during small temperature deviation step of 10 K over the 10 K did not cause any

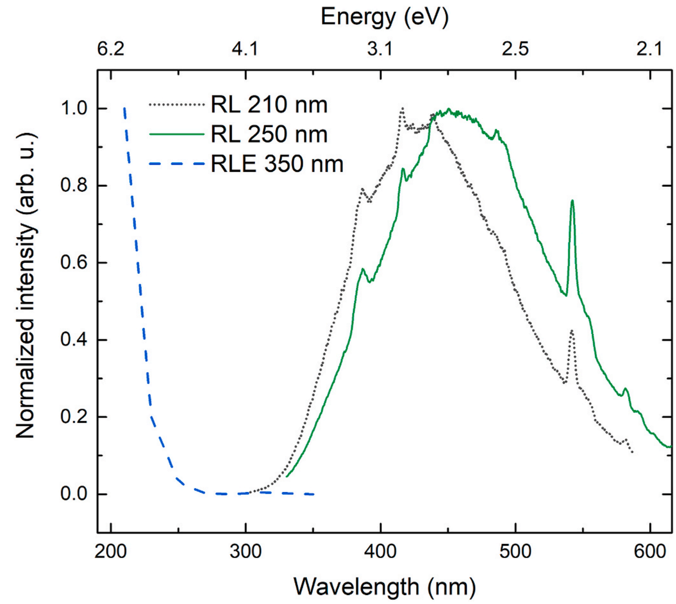

Fig. 3. RL spectra of the MYG garnet doped with 0.01 % Tb^{3+} after the excitation at 210 nm (dotted curve), 250 nm (solid curve) and 350 nm RL excitation spectrum (dashed curve) at 10 K.

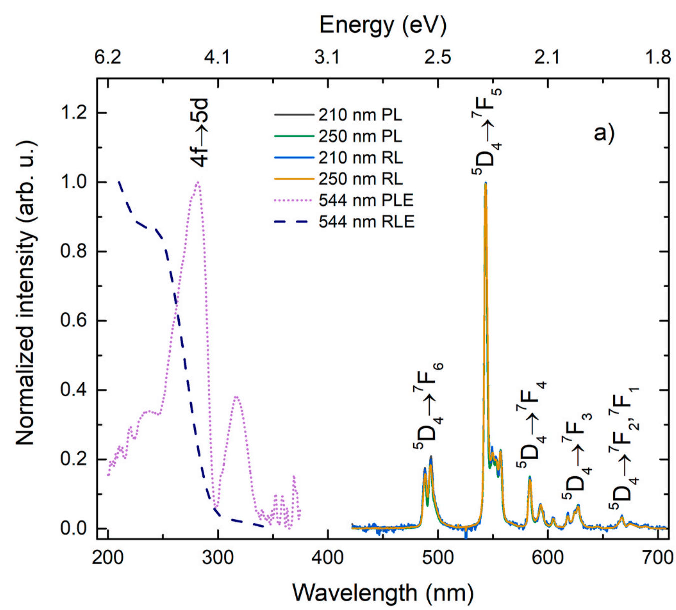

Fig. 4. Normalized PL and RL spectra of the MYG garnet doped with 10 % Tb^{3+} after the excitation at 210 and 250 nm, all 4 spectra coincide; PL excitation spectra at the Tb^{3+} lines at 544 nm (dotted curve) as well as the 544 nm RL excitation efficiency (dashed curve) measured at 10K.

intensity increase. This further strengthens the conclusion that temperature-dependent tunneling recombination is observed for both Tb concentrations at 10 K. The TSL peak at 250 K is from an unidentified charge traps which following UV irradiation is more pronounced in a high concentration Tb sample.

3.3. EPR

The normalized EPR spectra of the MYG:0.01 % Tb sample following exposure to UV radiation are shown in Fig. 7. In both cases of irradiation, EPR spectra were acquired using identical spectra acquisition settings; no signals were detected before the irradiation. The intensities and

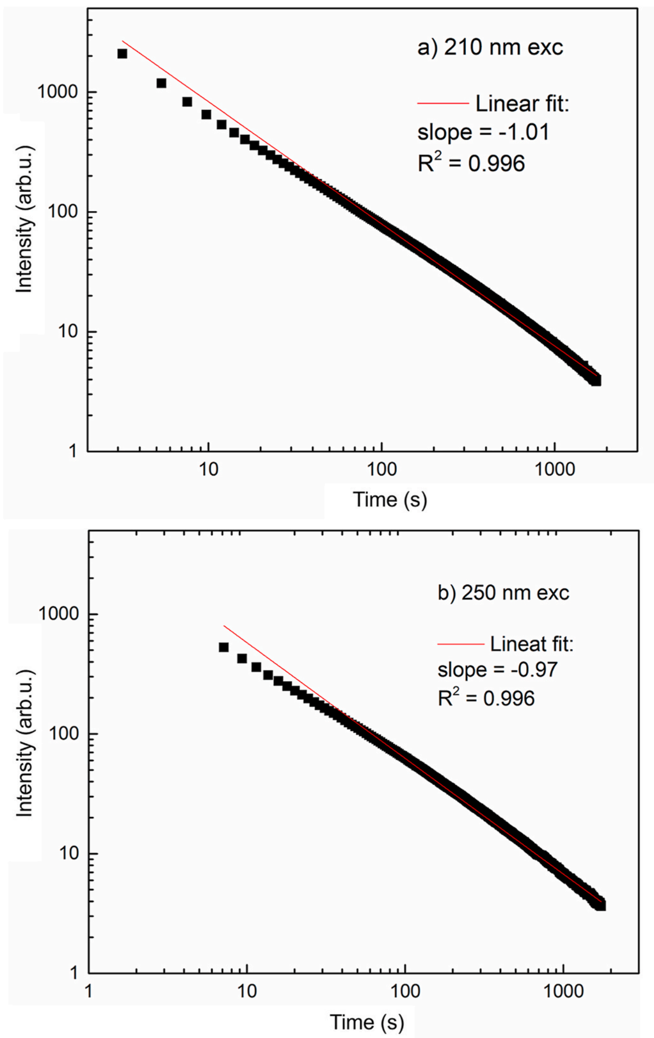

Fig. 5. Decay kinetics at T = 10 K of the integral RL of MYG garnet doped with 0.01 % Tb^{3+} after excitation at 210 nm (a) and with 10 % Tb^{3+} after excitation at 250 nm (b). Excitation time was 5 min.

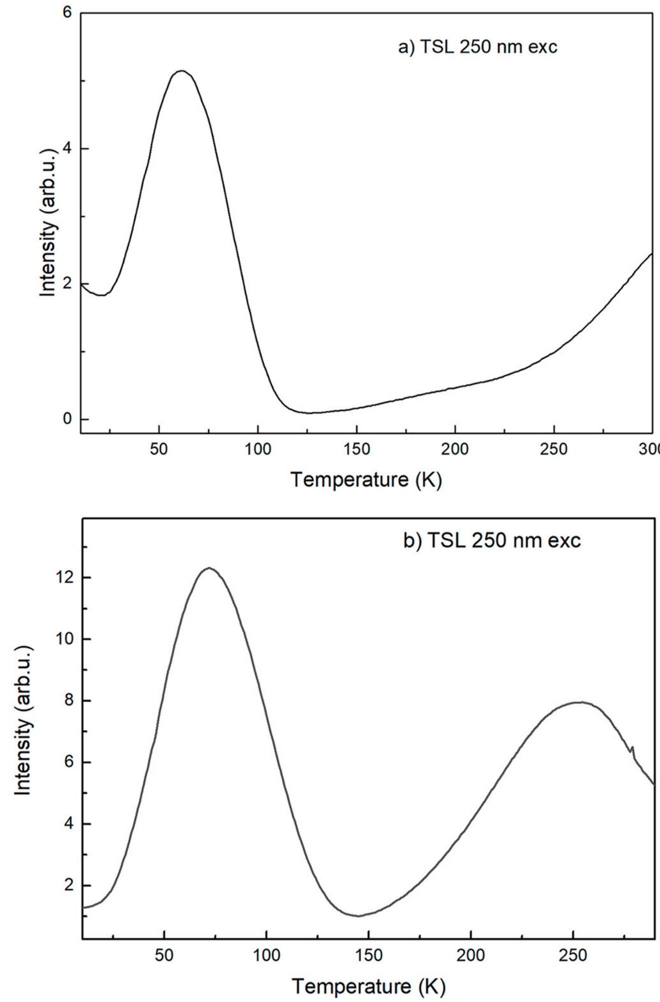

Fig. 6. TSL of the 0.01 % (a) and 10 % (b) Tb-doped MYG samples, measured by integral emission spectrum 30 min after the UV excitation at 10 K.

resonance positions of the UV-generated EPR signals are affected by the conditions of sample irradiation. Achieving uniform and effective irradiation of powder samples in the in-situ mode is problematic; thus resulting in a notable signal-to-noise ratio after the low-temperature sample irradiation. The variations of relative intensities suggest that the formation of specific paramagnetic centres depend on temperature, implying differences in charge carrier trapping and recombination mechanisms in MYG.

A simulation of the experimental spectrum after UV excitation at room temperature is presented in Fig. 8. The experimental spectrum can be simulated as a superposition of three components V(I), V(II), V(III) with SH parameter values reported in Ref. [15]. Different configurations of O^- ions in the MYG structure were proposed to be the most likely origin of the V-type centres. The thermal stability of the hole traps was found to correlate with TSL glow curves, providing evidence that these centres contribute to radiative recombination processes at temperatures above room temperature.

EPR spectra dependence on microwave power of the MYG: 0.01 % Tb sample after in-situ UV irradiation at 40 K is shown in Fig. 9. For a qualitative assessment, the g_{eff} axis (top) is introduced by using eq. (1) and the experimental microwave frequency. The highest-intensity resonances in the $2.00 < g_{eff} < 2.01$ range could partially be ascribed to the V(I) signal discussed above; however, the low field ($g_{eff} \approx 2.03$)

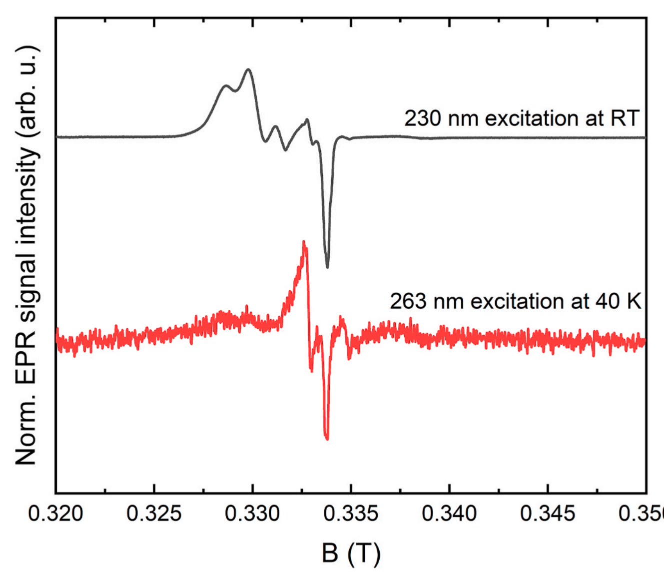

Fig. 7. Experimental EPR spectra of the MYG: 0.01 % Tb sample: upper trace – ex-situ 230 nm excitation at room temperature; lower trace – in-situ 263 nm excitation at 40 K.

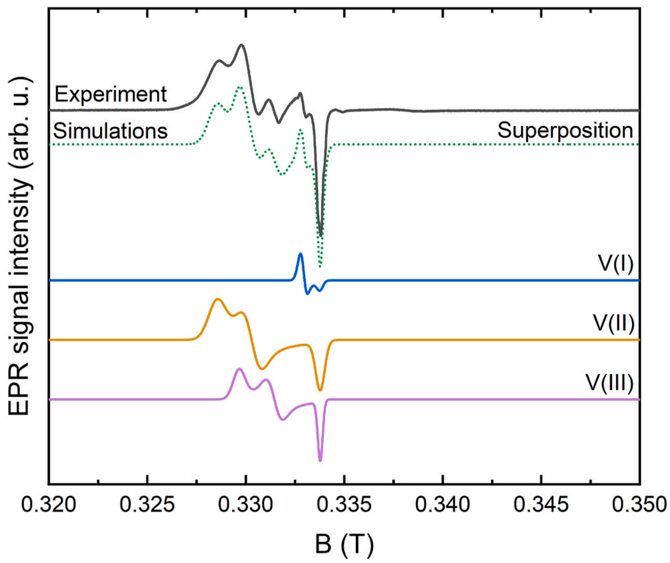

Fig. 8. EPR analysis of the MYG: 0.01 % Tb sample after UV excitation at room temperature: experimental spectrum (black trace); simulated spectra (green trace – superposition; blue trace – V(I) signal; yellow trace – V(II) signal; purple trace – V(III) signal).

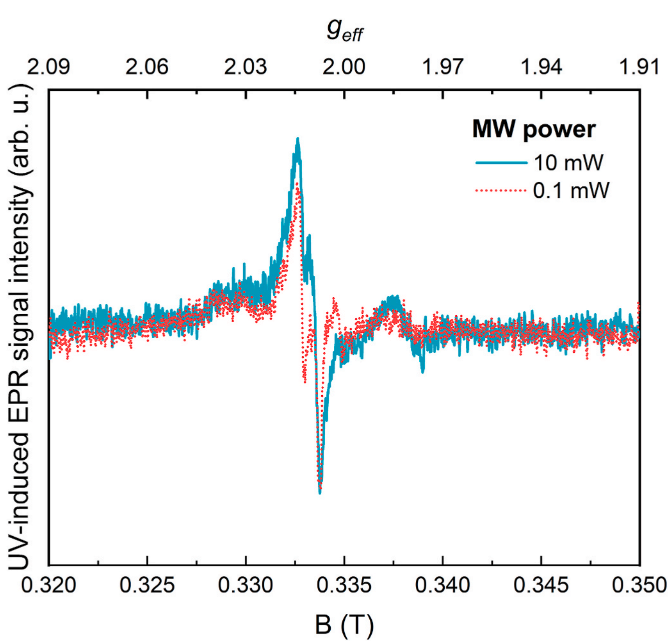

Fig. 9. Experimental EPR spectra of the 0.01 % Tb sample after UV excitation at 40 K acquired at different microwave (MW) power settings.

components of the V(II) and V(III) signals are barely discernible. There is a broad signal in the 1.97 < g_{eff} < 1.98 range, which becomes more pronounced at higher microwave power suggesting the generation of an additional F-type centre at low temperature. However, in many metal oxides, the intensity of the F^+ centre EPR absorption is maximal at low power values (0.1 mW or less) [33,34]. Thus, the observed power dependence in MYG may mean that the observed absorption belongs to a centre with a captured electron which is not necessarily the F^+ centre. The EPR results show that the excitation temperature influences UV-induced processes in MYG, possibly due to differences in the mechanisms of paramagnetic centre generation and their stabilities.

3.4. RL-EPR and PL-EPR

In order to find out information about the electron and hole centres participating in the broad PL and RL bands, RL-EPR and PL-EPR studies were performed on samples with low Tb concentration (0.01 %). The RL intensity of the broad 425–450 nm band at higher magnetic fields around 2.5–3 T was suppressed and thereafter partially restored at the resonance fields of participating hole/electron traps. The resulting resonance signals are shown in Fig. 10 for two microwave frequencies – 62.00 and 97.90 GHz.

The observed RL-EPR spectra were successfully fitted by assuming a recombination of one hole centre of S = ½ (V-type: g_1 = 2.035 ± 0.001; g_2 = 2.006 ± 0.001; g_3 = 2.001 ± 0.001) with one electron centre of S = ½ (F-type: g = 1.974 ± 0.001). The determined parameter values well-correlate with the EPR data after UV irradiation of the 0.01 % Tb doped sample at T = 40 K. For the attribution logic of these centres to F-type and V-type defects, see the EPR section above. The determined g-factor values of the V-type centres determined in the simulations of RL-EPR (Fig. 10) and EPR (Fig. 8) spectra overlap. It was confirmed that the RL-EPR resonances are observable for the entire broad RL band, using optical filters.

The second applied method – PL-EPR, in which microwaves were modulated with a frequency of 1 Hz during PL, gave resonance bands similar to the RL-EPR, only the signals of hole centres in the 2.18–2.21 T region were weaker than the signal of electron centres (see Fig. 11).

This could be explained by assuming that the hole centres have shorter relaxation times than electron centres. Thus, the PL and RL broadband spectra are not only similar in shape and position but also exhibit the same PL-EPR and RL-EPR resonance bands. We conclude that the observed PL and RL broad bands in MYG:Tb have similar origins – the tunneling recombination of electron and hole centres. Neither RL-EPR nor PL-EPR signals were found in the 10 % Tb-doped MYG sample.

3.5. RL mechanism of the Tb doped MYG at low temperatures

After UV excitation at 10 K of MYG:Tb, a small increase in temperature of over 10 K does not change the RL intensity and thermo-stimulated luminescence starts at about 20 K (Fig. 6). These observations and the hyperbolic RL quenching kinetics (Fig. 5) indicate that the low-temperature RL of MYG:Tb at both low (0.01 % Tb^{3+}) and high (10 % Tb^{3+}) concentrations is determined by the tunneling recombination of electron and hole centres.

The broad 425–450 nm RL band can be significantly suppressed by increasing the magnetic field up to 2–3 T. Then it can be largely restored by applying microwave radiation at the resonant magnetic fields of the electron or hole centres.

EPR measurements revealed signals of the electron and hole centres after the UV irradiation at 40 K (Fig. 9). RL-EPR has been observed only at low Tb^{3+} concentrations where the broad RL band dominates and the RL-EPR signals have the same parameters as in the EPR measurements. Therefore, the broad band RL is determined by the tunneling recombination of intrinsic electron (F-type) and hole (V-type) centres in MYG. The participation of intrinsic trap centres in RL is supported by the fact that RL efficiency grows by approaching the band gap value of MYG (see Fig. 3). For the MYG: Tb sample with low Tb^{3+} concentration, the Tb^{3+} lines could be observed as well, which may be caused by a partial energy transfer of the recombination energy to Tb^{3+} ions (Fig. 12a).

In contrast to MYG with the 0.01 % Tb, in the 10 % Tb-doped sample no broad band RL was observed and only Tb^{3+} lines could be detected in the PL and RL spectra (Fig. 4). RL has tunneling character and the decay is hyperbolic; therefore, the mechanism at 10 % Tb concentration should be related to the recombination between the electron and hole trap centres. As no broad RL bands could be detected, we suppose that at least one of the electron or hole centres would be different than at the RL-EPR at low Tb^{3+} concentration (Fig. 12b). The most likely centre with a trapped hole would be a Tb^{4+} centre. The presence of intrinsic electron/

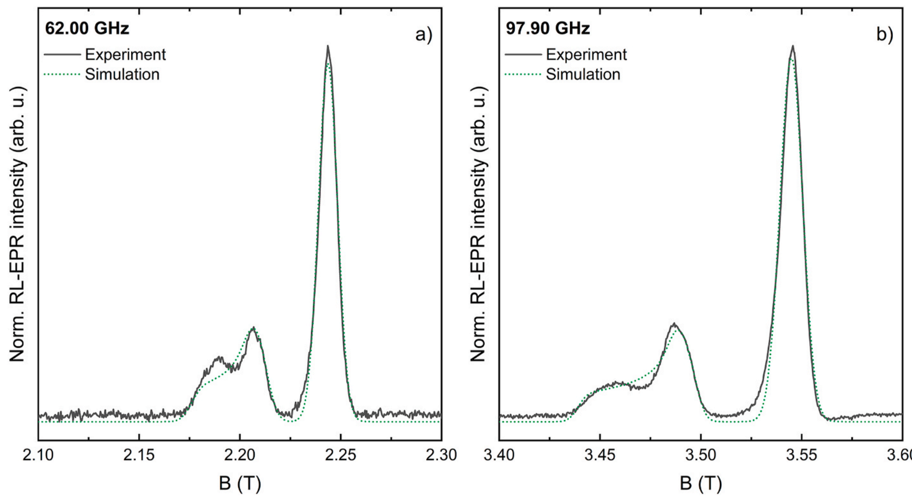

Fig. 10. RL-EPR spectra measured at T = 1.5 K and 62.00 (a) and 97.90 GHz (b) microwave frequencies and simulations using the EPR parameters (see the text below) of the corresponding hole centres (left group of lines) and electron trap centres (right line).

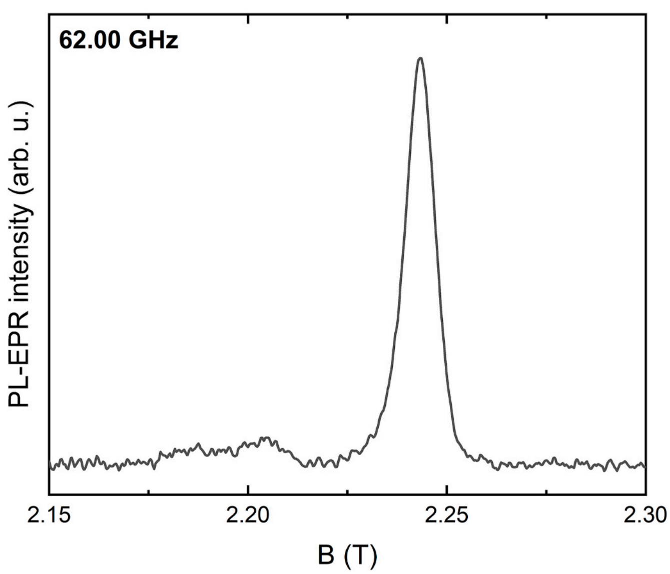

Fig. 11. PL-EPR spectrum measured at T = 1.5 K and 62 GHz microwave frequency.

or hole traps cannot be excluded as well, and the Tb^{3+} RL could be excited by wavelengths around the E_g value (Fig. 4, dashed line).

The band shape of the broad RL band is similar to the corresponding low-temperature PL band and is only slightly shifted to longer wavelengths (see Figs. 2 and 3) The PL-EPR spectrum shows the resonance lines of the same centres as present in the RL-EPR spectra. These similarities and the decay kinetics of PL suggest that the broad PL band of MYG:Tb at low Tb concentration has the same origin of the tunneling recombination of the intrinsic electron and hole centres as the broad RL band.

4. Conclusions

- Low-temperature PL and RL in MYG:Tb after UV irradiation at 210 nm or 250 nm show Tb^{3+} lines and, in case of low Tb^{3+} concentrations, an additional broad band at about 400–450 nm.
- The broad RL band has a long-lasting hyperbolic afterglow decay characteristic for tunneling recombination luminescence. The shape of the RL band is similar to the corresponding low-temperature PL band; however, it is shifted to longer wavelengths. The broad-band RL can be excited by photons with energies approaching the band gap of MYG. The decay kinetics and the similarity of the band shapes of the RL and PL spectra suggest that the broad PL and RL have the same origin: the tunneling recombination between intrinsic electron and hole centres.
- The broad RL band can be largely suppressed at low temperatures by magnetic field up to 3 T and restored by applying microwave radiation. RL-EPR spectra show resonances of both electron trap (F-type) and hole trap (V-type) centres.

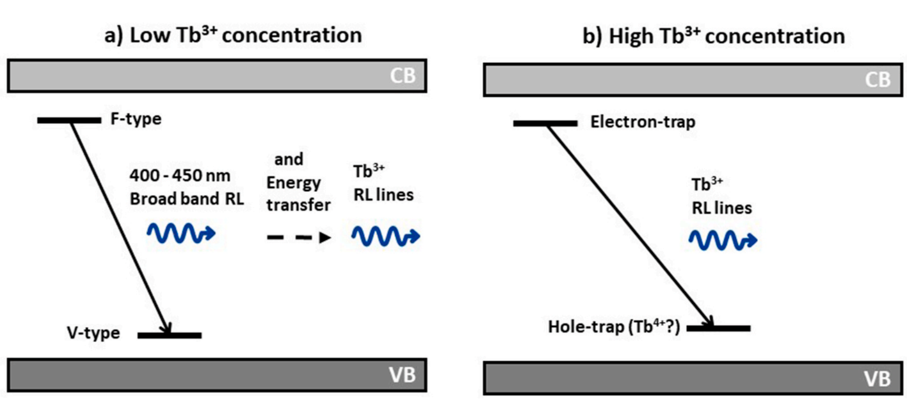

Fig. 12. Low-temperature RL mechanisms of the MYG:Tb.

- After UV irradiation at low temperature, electron and hole trap centres are observed in the EPR spectra. The g-factors of these paramagnetic centres correspond to those of RL-EPR signals.
- The Tb^{3+} RL lines appear either by transfer of recombination energy from the broad RL band to the Tb^{3+} absorption bands (for low Tb concentration) or tunneling recombination of electron trap and hole (probably Tb^{4+}) centres (for high Tb concentration).

CRediT authorship contribution statement

U. Rogulis: Writing – review & editing, Conceptualization. **A. Fedotovs:** Methodology, Investigation, Formal analysis. **Dz Berzins:** Methodology. **G. Krieke:** Writing – original draft, Investigation, Conceptualization. **L. Skuja:** Methodology. **A. Antuzevics:** Writing – original draft, Project administration, Investigation, Formal analysis.

Declaration of competing interest

The authors declare that they have no known competing financial interests or personal relationships that could have appeared to influence the work reported in this paper.

Data availability

No data was used for the research described in the article.

Acknowledgements

This research is funded by the Latvian Council of Science, project “Defect engineering of novel UV-C persistent phosphor materials”, Project no. lzp-2021/1–0118.

Institute of Solid State Physics, University of Latvia as the Centre of Excellence has received funding from the European Union’s Horizon 2020 Framework Programme H2020-WIDESPREAD-01-2016-2017-TeamingPhase2 under grant agreement No. 739508, project CAMART^2.

References

[1] J. Hölsä, Persistent luminescence beats the afterglow: 400 Years of persistent luminescence, Electrochem. Soc. Interface 18 (2009) 42, https://doi.org/10.1149/2.F06094IF.
[2] N. Thejo Kalyani, A. Jain, S.J. Doble, Persistent phosphors for luminous paints: a review, Luminescence 37 (2022) 524–542, https://doi.org/10.1002/bio.4203.
[3] J. Zhao, L. Lei, R. Ye, J. Ahang, X. Zhang, S. Xu, Sunlight activated ultra-stable long persistent luminescence glass ceramic for outdoor information display, Journal of Advanced Ceramics 11 (2022) 974–983, https://doi.org/10.1007/s40145-022-0595-1.
[4] J. Liu, T. Lécuyer, J. Seguin, N. Mignet, D. Scherman, B. Viana, C. Richard, Imaging and therapeutic applications of persistent luminescence nanomaterials, Adv. Drug Deliv. Rev. 138 (2019) 193–210, https://doi.org/10.1016/j.addr.2018.10.015.
[5] S. Wu, Y. Li, W. Ding, L. Xu, Y. Ma, L. Zhang, Recent advances of persistent luminescence nanoparticles in bioapplications, Nano-Micro Lett. 70 (2020) 1–26, https://doi.org/10.1007/s40820-020-0404-8.
[6] A. Bessière, J.-O. Durand, C. Noûs, *Nanophotonics*, Persistent Luminescence Materials for Deep Photodynamic Therapy, vol. 10, 2021, pp. 2999–3029, https://doi.org/10.1515/nanoph-2021-0254.
[7] D.L. Fritzen, L. Giordano, L.C.V.V. Rodrigues, J.H.S.K. Monteiro, Opportunities for persistent luminescent nanoparticles in luminescence imaging of biological systems and photodynamic therapy, Nanomaterials 10 (2020) 2015, https://doi.org/10.3390/nano10102015.
[8] Yu Zorenko, T. Voznyak, V.V. Gorbenko, A. Doroshenko, A. Tolmachev, R. Yavetskiy, I. Petrusha, V. Turkevich, Comparative study of the luminescence of $Y_3Al_5O_{12}$ nanoceramics and single crystals under excitation by synchrotron radiation, Opt. Mater. 35 (2013) 2049–2052, https://doi.org/10.1016/j.optmat.2012.07.009.
[9] Zh T. Karipbayev, V.M. Lisitsyn, D.A. Mussakhanov, G.K. Alpyssova, A.I. Popov, E. F. Polosadova, E. Elsts, A.T. Akilbekov, A.B. Kukenova, M. Kemere, A. Sarakovskis, A. Lushchik, Time-resolved luminescence of YAG: Ce and YAGG: Ce ceramics prepared by electron beam assisted synthesis, Nucl. Instrum. Methods Phys. Res. Sect. B Beam Interact. Mater. Atoms 479 (2020) 222–228, https://doi.org/10.1016/j.nimb.2020.06.046.
[10] N. Mironova-Ulmane, A.I. Popov, A. Antuzevics, G. Krieke, E. Elsts, E. Vasil’chenko, I. Sildos, L. Puust, S.B. Ubizskii, D. Sugak, V. Skvortsova, A. Dauletbekova, K. Kumarbekov, A. Sarakovskis, EPR and optical spectroscopy of neutron-irradiated $Gd_3Ga_5O_{12}$ single crystals, Nucl. Instrum. Methods Phys. Res. Sect. B Beam Interact. Mater. Atoms 480 (2020) 22–26, https://doi.org/10.1016/j.nimb.2020.07.024.
[11] Y. Fujimoto, T. Yanagida, H. Yagi, T. Yanagidani, V. Chani, Comparative study of intrinsic luminescence in undoped transparent ceramic and single crystal garnet scintillators, Opt. Mater. 36 (2014) 1926–1929, https://doi.org/10.1016/j.optmat.2014.06.019.
[12] M. Baran, A. Kissabekova, A. Krasnikov, A. Reszka, L. Vasilechko, S. Zazubovich, Ya Zhydachevskyy, Luminescence and defects creation processes in Bi^{3+}-doped gallium garnets, J. Lumin. 253 (2023) 119483, https://doi.org/10.1016/j.jlumin.2022.119483.
[13] A. Vedda, M. Fasoli, Tunneling recombinations in scintillators, phosphors, and dosimeters, Radiat. Meas. 118 (2018) 86–97, https://doi.org/10.1016/j.radmeas.2018.08.003.
[14] B. Padlyak, The nature of intrinsic luminescence in glasses and crystals of CaO-Ga_2O_3-GeO_2 system, Ukr. J. Phys. Opt. 8 (2007) 235–248, https://doi.org/10.3116/16091833/8/4/235/2007.
[15] G. Krieke, G. Doke, A. Antuzevics, I. Pudza, A. Kuzmin, E. Welter, Tuneable persistent luminescence of novel $Mg_3Y_2Ge_3O_{12}$ garnet, J. Alloys Compd. 922 (2022) 166312, https://doi.org/10.1016/j.jallcom.2022.166312.
[16] D. Lévy, J. Barbier, Normal and inverse garnets: $Ca_3Fe_2Ge_3O_{12}$, $Ca_3Y_2Ge_3O_{12}$ and $Mg_3Y_2Ge_3O_{12}$, Acta Crystallogr. Sect. C Cryst. Struct. Commun. 55 (1999) 1611–1614, https://doi.org/10.1107/S0108270199007854.
[17] C. Ji, Z. Huang, X. Tian, H. He, J. Wen, Y. Peng, Novel red emitting phosphors $Mg_3Y_2Ge_3O_{12}$:Sm^{3+} with high color purity and excellent thermal stability used in W-LEDs, J. Alloys Compd. 825 (2020) 154176, https://doi.org/10.1016/j.jallcom.2020.154176.
[18] M. Liao, Z. Mu, S. Zhang, F. Wu, Z. Nie, Z. Zheng, X. Feng, Q. Zhang, J. Feng, D. Zhu, A red phosphor $Mg_3Y_2Ge_3O_{12}$: Bi^{3+}, Eu^{3+} with high brightness and excellent thermal stability of luminescence for white light-emitting diodes, J. Lumin. 210 (2019) 202–209, https://doi.org/10.1016/j.jlumin.2019.02.038.
[19] J. Zhou, R. Wang, T. Jiao, Z. Bai, X. Wang, Y. Guo, Q. Zhang, Q. Peng, $Mg_3Y_2Ge_3O_{12}$:Bi^{3+}, UV fluorescent phosphor as the TiO_2 “sensitizer” for enhancing the heavy oil viscosity reduction, Ceram. Int. 45 (2019) 13112–13118, https://doi.org/10.1016/j.ceramint.2019.03.245.
[20] Z. Jiang, Y. Wang, L. Wang, Enhanced yellow-to-orange emission of Si-doped $Mg_3Y_2Ge_3O_{12}$:Ce^{3+} garnet phosphors for warm white light-emitting diodes, J. Electrochem. Soc. 157 (2010) J155–J158.
[21] H. Lin, J. Xu, Q. Huang, B. Wang, H. Chen, Z. Lin, Y. Wang, Bandgap tailoring via Si doping in inverse-garnet $Mg_3Y_2Ge_3O_{12}$:Ce^{3+} persistent phosphor potentially applicable in AC-LED, Appl. Mater. Interfaces 7 (2015) 21835–21843, https://doi.org/10.1021/acsami.5b06071.
[22] N.G. Romanov, Y.P. Veshchunov, V.A. Vetrov, P.G. Baranov, Application of tunneling recombination afterglow for EPR optical detection of recombining centres in ionic crystals, Phys. Status Solidi. 107 (1981) K119–K124, https://doi.org/10.1002/pssb.2221070255.
[23] U. Rogulis, J.M. Spaeth, I. Tale, M. Nikl, N. Ichinose, K. Shimamura, Magnetooptical studies of defects and recombination luminescence in $LiBaF_3$, Radiat. Meas. 38 (2004) 663–666, https://doi.org/10.1016/j.radmeas.2004.03.013.
[24] M. Secu, S. Schweizer, U. Rogulis, J.M. Spaeth, Radiation-induced defects and their recombination processes in the x-ray storage phosphor $BaBr_2$:Eu^{2+}, J. Phys. Condens. Matter 15 (2003) 2061–2070, https://doi.org/10.1088/0953-8984/15/12/323.
[25] U. Rogulis, G. Krieke, A. Antuzevics, A. Fedotovs, Dz Berzins, A.I. Popov, V. Pankratov, Low-temperature recombination luminescence of La-doped Ca_2SnO_4, Opt. Mater. 129 (2022) 112545, https://doi.org/10.1016/j.optmat.2022.112545.
[26] S. Stoll, A. Schweiger, EasySpin, a comprehensive software package for spectral simulation and analysis in EPR, J. Magn. Reson. 178 (2006) 42–55, https://doi.org/10.1016/j.jmr.2005.08.013.
[27] J.A. Weil, J.R. Bolton, Electron Paramagnetic Resonance, Wiley, 2007.
[28] M.J. Oh, S. Saha, H.J. Kim, The luminescence properties of Sm^{3+} or Tb^{3+} –doped $Lu_3Ga_2Al_3O_{12}$ phosphors for X-ray imaging, J. Kor. Phys. Soc. 75 (2019) 957–961, https://doi.org/10.3938/jkps.75.957.
[29] J.C.A. Santos, E.P. Silva, N.R.S. Souza, Y.G.S. Alves, D.V. Sampaio, C. Kucera, L. G. Jacobsohn, J. Ballato, R.S. Silva, Laser sintering and photoluminescence study of Tb-doped yttrium aluminium garnet ceramics, Ceram. Int. 45 (2019) 3797–3802, https://doi.org/10.1016/j.ceramint.2018.11.048.
[30] Z. Li, B. Zhong, Y. Cao, S. Zhang, Y. Lv, Z. Mu, Z. Hu, Y. Hu, Energy transfer and luminescence properties of $Y_3Al_2Ga_3O_{12}$:Tb^{3+},Sm^{3+} as a multi-colour emitting phosphors, J. Mater. Sci. Mater. Electron. 30 (2019) 10491–10498, https://doi.org/10.1007/s10854-019-01392-z.
[31] C.J. Delbecq, D.L. Dexter, P.H. Yuster, Tunneling-recombination luminescence between Ag^0 and Ag^{2+} in KCl:AgCl, Phys. Rev. B 17 (1978) 4765–4774, https://doi.org/10.1103/PhysRevB.17.4765.
[32] T. Tashiro, S. Takeuchi, M. Saidoh, N. Itoh, Luminescence induced by tunnelling recombination between neutral silver atoms and V_K centres in alkali halides, Phys. Status Solidi 92 (1979) 611–618, https://doi.org/10.1002/pssb.2220920234.
[33] V. Seeman, A.I. Popov, E. Shablonin, E. Vasil’chenko, A. Lushchik, EPR-active dimer centers with S = 1 in α-Al_2O_3 single crystals irradiated by fast neutrons, J. Nucl. Mater. 569 (2022) 153933, https://doi.org/10.1016/j.jnucmat.2022.153933.
[34] A. Antuzevics, E. Elsts, M. Kemere, A. Lushchik, A. Moskina, Th A. Scherer, A. I. Popov, Thermal annealing of neutron irradiation generated paramagnetic defects in transparent Al_2O_3 ceramics, Opt. Mater. 135 (2023) 113250, https://doi.org/10.1016/j.optmat.2022.113250.